CHEMISTRY

10.1126/sciadv.1500421

A single-ligand ultra-microporous MOF for precombustion CO_2 capture and hydrogen purification

Shyamapada Nandi,[1] Phil De Luna,[2] Thomas D. Daff,[2] Jens Rother,[3] Ming Liu,[4] William Buchanan,[5] Ayman I. Hawari,[4] Tom K. Woo,[2]* Ramanathan Vaidhyanathan[1,5]*

Metal organic frameworks (MOFs) built from a single small ligand typically have high stability, are rigid, and have syntheses that are often simple and easily scalable. However, they are normally ultra-microporous and do not have large surface areas amenable to gas separation applications. We report an ultra-microporous (3.5 and 4.8 Å pores) Ni-(4-pyridylcarboxylate)$_2$ with a cubic framework that exhibits exceptionally high CO_2/H_2 selectivities (285 for 20:80 and 230 for 40:60 mixtures at 10 bar, 40°C) and working capacities (3.95 mmol/g), making it suitable for hydrogen purification under typical precombustion CO_2 capture conditions (1- to 10-bar pressure swing). It exhibits facile CO_2 adsorption-desorption cycling and has CO_2 self-diffusivities of ~3 × 10^{-9} m^2/s, which is two orders higher than that of zeolite 13X and comparable to other top-performing MOFs for this application. Simulations reveal a high density of binding sites that allow for favorable CO_2-CO_2 interactions and large cooperative binding energies. Ultra-micropores generated by a small ligand ensures hydrolytic, hydrostatic stabilities, shelf life, and stability toward humid gas streams.

INTRODUCTION

Coal-fired power plants currently generate approximately 40% of the world's electricity and are one of the largest sources of anthropogenic CO_2 emissions worldwide (*1*, *2*). To mitigate the greenhouse gas emissions of power generation, postcombustion CO_2 capture technologies have attracted significant attention (*3*, *4*). However, alternatives to directly burning coal and scrubbing CO_2 from the combustion gas exist that may be more efficient and ultimately less costly (*5*, *6*). Coal gasification is expected to be a key technology for future clean coal power and involves the catalytic steam reforming of the fuel to produce a high-pressure H_2/CO_2 gas mixture (*6*–*8*). CO_2 is then separated from the mixture, resulting in a near-pure H_2 stream that can be burned to produce water as the only combustion product. Currently, more than 90% of the world's hydrogen is produced from gasification (*9*). In these industrial processes, pressure swing adsorption (PSA) systems with solid sorbents, such as zeolite 13X or activated carbon, are used to separate the CO_2 from the H_2 (*10*–*12*). However, the gas separation process is still too energy-demanding for large-scale coal gasification power plants to be commercially viable, and further optimization of the purification process is required (*7*, *10*–*12*). Although process tuning will play a large role in this optimization, the largest opportunities lie in materials development of the solid sorbents.

Metal organic frameworks (MOFs) with large surface areas have attracted attention as solid sorbents for large-scale gas separation applications (*13*–*16*). They have been intensively studied for CO_2 capture from combustion flue gases where CO_2/N_2 gas separations at low pressure are pertinent (*3*, *4*, *16*–*22*). Despite the potential application for coal gasification, reports of MOFs for high-pressure CO_2/H_2 separations have been limited (*23*–*27*). Recently, Long and coworkers examined a variety of well-known MOFs and identified Mg_2(dobdc) and Cu-BTTri as the most promising candidates for CO_2/H_2 separations because they were found to have high CO_2/H_2 adsorption selectivities and large CO_2 working capacities under PSA conditions relevant to coal gasification (*23*). Notably, both of these MOFs have metal sites with unsaturated coordination or so-called open metal sites. Although the open metal sites are advantageous in establishing strong and selective CO_2 binding, they could be problematic in terms of long-term hydrolytic stability. Unsaturated metal sites, which are strong Lewis acids, tend to readily interact with even trace quantities of water, resulting in either diminished adsorption properties or irreversible degradation of the materials (*28*–*30*). This is problematic for practical gas separations because the complete removal of water following steam reforming during coal gasification is not practical.

Recently, ultra-microporous MOFs (pores in the range of 4 to 6 Å) with exceptional postcombustion CO_2 capture capabilities have been demonstrated (*21*, *31*, *32*). Ultra-microporous MOFs have some structural advantages that make them excellent gas separation sorbents. For example, the small pores can facilitate strong framework-gas interactions and can enhance the cooperative effects between the adsorbed species (*32*). They also have inherent molecular sieving capabilities. In terms of stability, the small ligands tend to give rise to rigid structures and improved shelf life when compared to the MOFs built from large organic ligands (*33*–*36*). We note that some exceptionally stable large-pore MOFs have been reported (*33*, *37*–*40*). Ultra-microporous materials typically have relatively low saturation limits at high pressure, which has made them unattractive targets for PSA applications. At high pressure, large pores can allow the guest molecules to pack densely, resulting in high uptake capacities that are important for gas separation applications. Thus, obtaining high uptake capacities at high pressures from ultra-microporous MOFs is seemingly paradoxical and remains a challenge.

[1]Department of Chemistry, Indian Institute of Science Education and Research, Pune 411008, India. [2]Centre for Catalysis Research and Innovation, Department of Chemistry, University of Ottawa, Ottawa, Ontario K1N 6N5, Canada. [3]Institute of Thermo and Fluid Dynamics, Ruhr-University Bochum, Universitätsstraße 150, D-44801 Bochum, Germany. [4]Department of Nuclear Engineering, North Carolina State University, Raleigh, NC 27695, USA. [5]Enovex Technology Corporation, Saint John, New Brunswick E2L 2E9, Canada.
*Corresponding author. E-mail: vaidhya@iiserpune.ac.in (R.V.); twoo@uottawa.ca (T.K.W.)

Here, we report a 4-pyridylcarboxylate–based ultra-microporous MOF [Ni-4PyC, $Ni_9(\mu\text{-}H_2O)_4(H_2O)_2(C_6NH_4O_2)_{18}$.solvent], **1**, with unusually high CO_2 saturation capacity (8.2 mmol/g) and exceptional CO_2/H_2 selectivity at high pressure. The material is also moisture-stable and has favorable CO_2 diffusion coefficients and modest heats of adsorption (HOA) for low energy cycling under PSA conditions (*41*). **1** is also straightforwardly made in a one-pot synthesis from a single metal and single small, readily available ligand, allowing for easy scale-up (*42*). We have examined the gas adsorption properties of **1** for CO_2/H_2 gas separations and explored the origin of the unusually high CO_2 uptake by probing the nature of adsorption sites via simulations.

RESULTS

The structure of **1**, shown in Fig. 1A, is built up from corner-sharing nickel dimers and isolated octahedral nickel centers (figs. S1 and S2). There are two such nickel dimers, one built up from Ni(1) and Ni(2) atoms and the other from Ni(3), that are coordinated by 4PyC units and water molecules (terminal and bridging). The μ-2 water-bridged Ni dimers (*43*, *44*) form the building units of **1**, which are different from the μ-3 hydroxo-bridged Ni clusters (*45*–*47*) reported in the literature. If the dimers are reduced to a node and the PyC moieties to linear linkers, the structure is a six-connected cubic network (Fig. 1). This three-dimensional (3D) framework consists of two types of channels and a cage system. Of the two channels, one is one-dimensionally aligned along the *c* axis (~6.7 × 6.7 Å—dimensions in this article refer to those measured from the nuclear positions and do not account for the van der Waals radii). The other channel exhibits two-dimensional accessibility along both *a* and *c* axes (7.8 × 7.8 Å and 7.5 × 7.5 Å), and four such channels surround the aforementioned one-dimensional channel. The access to the one-dimensional channels from the *a* and *b* axes is blocked by the cages in the structure, which are made up of the same nickel dimers that line the one-dimensional channels. These dimers are arranged into a square and are capped by two isolated nickel octahedra, Ni(5), on either side to generate the near-spherical cage (12 × 12 × 12 Å). Topologically, the channel system in **1** is composed of alternating 2D and the 1D channels stacked long the *b* axis (Fig. 1B). The carboxylate groups and bridging water molecules lining the channels impart a polar character to them. The ditopic PyC units were strongly disordered, making the structure solution challenging; however, they could be modeled using a head-tail orientation. Obtaining the correct minimized geometry via disorder modeling was crucial to obtaining the correct chemical composition.

The N_2 adsorption isotherm at 77 K is given in Fig. 2A and yields a Brunauer, Emmett, and Teller (BET) surface area of 945 m^2/g. Despite the modest surface area, 195-K uptake is notably higher than that of most other ultra-microporous MOFs (table S1). Figure 2B depicts the CO_2 adsorption isotherms over a range of temperatures with a total uptake of 11, 5.5, and 3.6 mmol/g at 195, 273, and 303 K, at 1 bar, respectively. The density functional theory (DFT) model of the 195-K CO_2 adsorption branch indicated a bimodal pore distribution in the ultra-microporous regime (3.5 and 4.8 Å, fig. S11). A positron annihilation lifetime spectroscopy (PALS) measurement was also carried out to establish the ultra-microporous character of **1** (*48*). The PALS was recorded on a MeOH exchanged sample that was activated at 100°C for 24 hours (Supplementary Materials). The spectra were least-squares fit with the program PosFit (fig. S12) (*49*), using three lifetime components, as shown in table S3. The fit to the 1.2- to 1.4-ns component of the ortho-positronium (o-Ps) annihilation yielded a spherical pore size of 3.9 to 4.4 Å, which is fairly consistent with the values obtained from the single-crystal structure of **1** and from the 195-K CO_2 data.

The CO_2 HOA in **1** were determined via both virial fits and a DFT model using isotherms collected at −25°, −10°, 0°, +10°, and +30°C. The virial fit presented in Fig. 2C shows that **1** has the zero-loading HOA value of 34 kJ/mol and this falls down to a value of 26 at ~2 mmol/g loading and settles down at a moderate 28 kJ/mol at higher loadings. Both models showed a similar trend (fig. S13).

For an ultra-microporous material, **1** has an exceptionally high CO_2 saturation capacity of 10.8 mmol/g (195 K), which suggested that it may also have a high CO_2 uptake capacity at high pressure and high temperature—conditions relevant to precombustion H_2 purification. The adsorption pressure of PSA systems used in precombustion CO_2 capture is typically 5 to 40 bar and occurs at elevated temperatures usually around 40°C (*12*, *23*). To explore this, we first performed grand

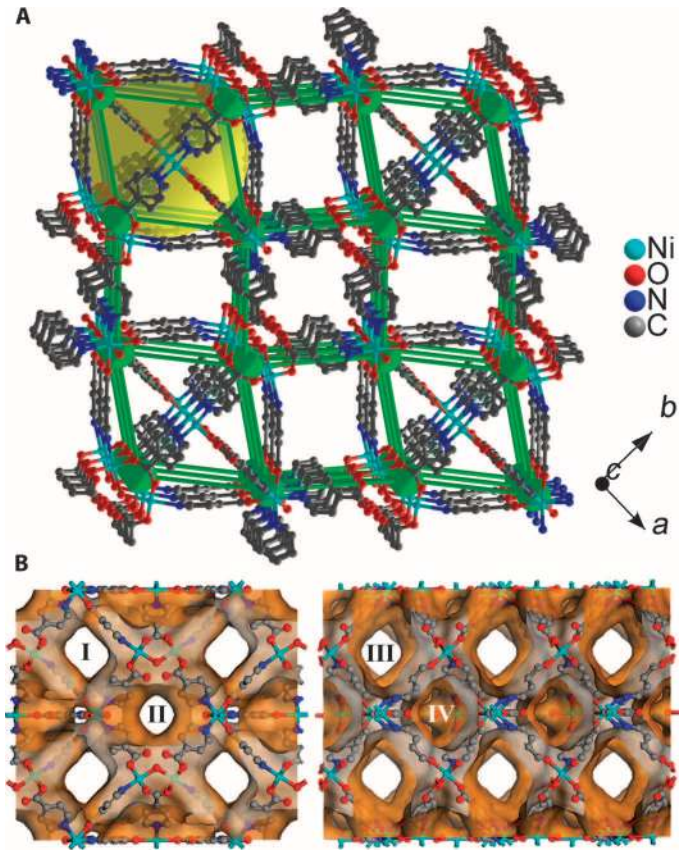

Fig. 1. Nanoporous structure of 1. (**A**) Single-crystal x-ray structure of **1** generated using OLEX; green, Ni dimers reduced to one node. The green cones trace the six-connected distorted cubic arrangement formed by collapsing the Ni dimers to nodes and the PyC linkers as lines. The yellow ball represents the cages in the structure. (**B**) The Connolly surface diagram of **1** (probe radius, 1.4 Å) showing the 2D and 1D channels. The channels labeled I and III are interconnected and run along the *a* and *c* axes, respectively, whereas the channel labeled II is truly one-dimensional along the *c* axis. IV represents the cages in **1**, which are lined with terminal water molecules in addition to the ligand groups.

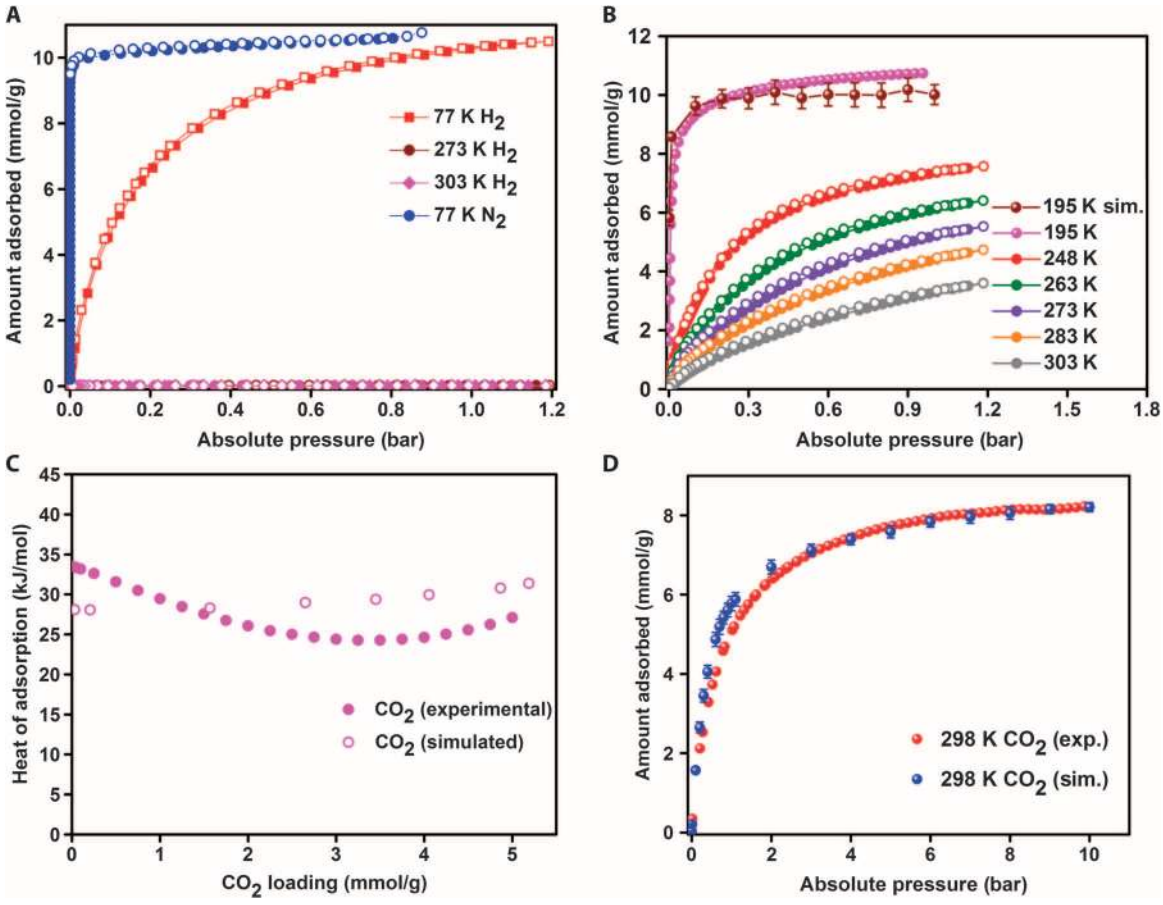

Fig. 2. Experimental and simulated adsorption isotherms and HOA plots. (**A**) Experimental H_2 and N_2 isotherms. (**B**) CO_2 adsorption isotherms carried out on **1** at different temperatures (filled circles, adsorption; open circles, desorption). For CO_2 at 195 K, the simulated adsorption isotherm is shown. (**C**) HOA for CO_2 in **1** as a function of the CO_2 loading determined from a virial fit to isotherms collected at temperatures ranging from −25° to 30°C. HOA determined from GCMC simulations at 25°C are also shown. (**D**) Experimental and simulated gas adsorption isotherms for CO_2 at 298 K (0 to 10 bar).

canonical Monte Carlo (GCMC) simulations (see the Supplementary Materials for details), which predicted a high uptake capacity of 8.2 mmol/g at 10 bar and 298 K. Because the simulated and experimental HOA and 195-K CO_2 adsorption isotherms were in good agreement with one another (Fig. 2, B and C), this inspired us to measure the high-pressure CO_2 adsorption. Figure 2D reveals that the simulated and experimental CO_2 adsorption between 1 and 10 bar and 298 K are in excellent agreement. In addition, the high-pressure H_2 adsorption revealed that **1** did not show any appreciable H_2 uptake even at 35 bar (fig. S16).

For an ultra-microporous material, the exceptional CO_2 uptake capacity of **1** near the saturation limits demands a molecular-level investigation of the adsorption sites to understand how **1** can accommodate such a large amount of CO_2. To study this, we examined the nature and location of the binding sites within Ni-4PyC via simulation. The GCMC simulations that are used to generate the adsorption isotherms also yield probability distributions of the guest molecules that can be used to locate the binding sites. We have performed a similar analysis on a ZnAtzOx MOF and found there to be excellent agreement between the computed CO_2 binding sites and those determined from crystallography (*32*). The low temperature saturation limit of 10.8 mmol/g determined experimentally corresponds to approximately 28 CO_2 molecules per unit cell. Figure 3 shows the location of the strongest 30 binding sites, with binding energies ranging from −24.0 to −32.8 kJ/mol. These were calculated by geometry optimizing a single CO_2 molecule in the empty MOF, starting from the CO_2 position identified from the maxima of the probability distributions. Three main binding site regions were identified in this way and encompass the main channels and cages previously described. The first region, labeled I/III in Fig. 3, is contained within the intersection of channels I and III (Fig. 1). The second binding region labeled II is located within the 1D channel system first shown in Fig. 1. The third binding region contains the previously mentioned spherical cages, which are labeled region IV. The accessible surface area (calculated with a CO_2 probe radius) drops from 1194 m^2/g in the empty MOF to <1 m^2/g in the MOF with the 28 lowest-energy CO_2 binding sites occupied, demonstrating almost full saturation within **1**. Binding region IV has the strongest binding sites that are sandwiched between the aromatic planes of two PyC ligands, with binding energies ranging from −30.0 to −32.8 kJ/mol. The weakest binding sites are found in region II and have binding energies of −24.0 to −27.2 kJ/mol. The binding in this region was found to have virtually no electrostatic component—that is, the binding was due almost entirely to dispersion interactions. This contrasts the binding sites in the other two regions (I/III and IV)

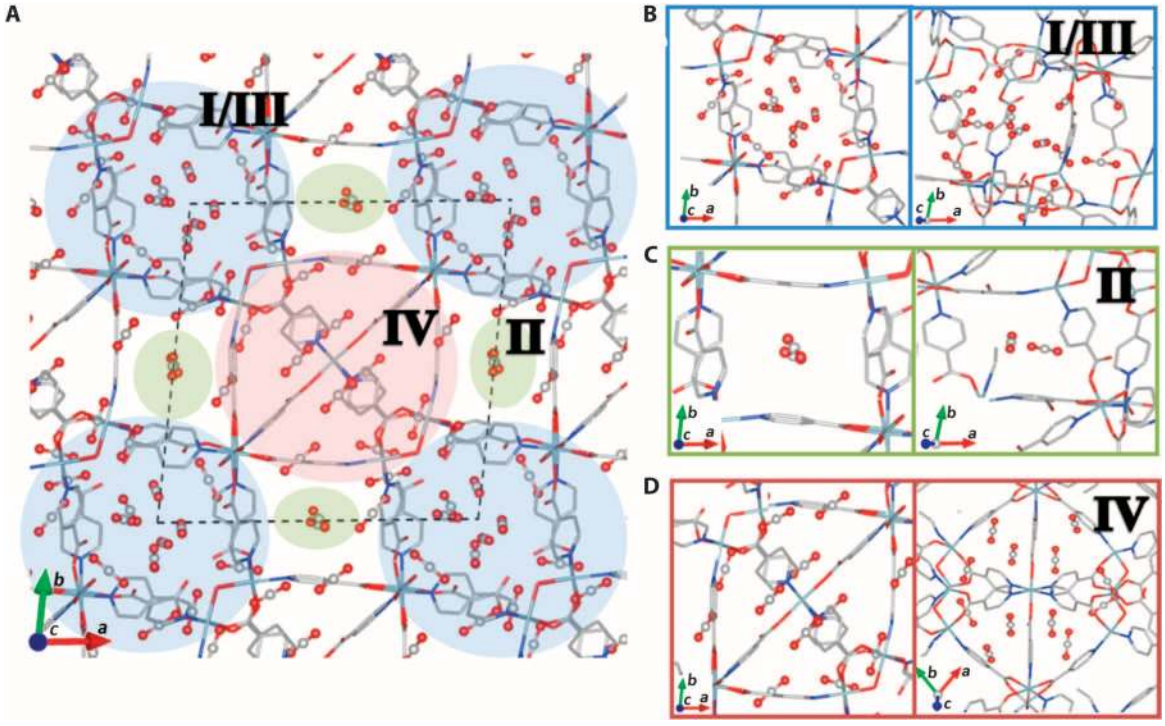

Fig. 3. CO_2 binding sites modeled from simulations. (**A**) A view looking down the *c* axis of **1** showing the top 30 CO_2 binding sites determined from a GCMC simulation at 195 K and 1 bar. There are three distinct binding regions noted in blue (I/III), green (II), and red (IV). Binding region I/III corresponds to the 2D channels depicted in Fig. 1B. Binding region II corresponds to the 1D channels labeled II in Fig. 1B. IV corresponds to the near-spherical cage. (**B** to **D**) Close-ups and different views of binding regions. (B) I/III. (C) II. (D) IV.

whose binding energies were composed of up to 22% electrostatic interactions.

With a high density of binding sites, one might expect to see cooperative binding effects where bound guest molecules interact favorably with one another. By occupying the 28 most stable binding sites with CO_2, we find that there is a significant cooperative binding energy of 5.2 kJ/mol per guest molecule. That is, with the 28 binding sites occupied, there is a net stabilization of 146 kJ/mol due to favorable CO_2-CO_2 interactions. After 29 guest molecules (just beyond the low temperature saturation limit), the cooperative binding energy begins to diminish as additional CO_2 molecules interact unfavorably with existing guest molecules (*50*). These results suggest that cooperative binding plays a significant role in the high CO_2 uptake capacities observed in **1**.

To more thoroughly explore the potential of **1** for precombustion CO_2 capture, binary mixtures of CO_2 and H_2 were simulated at 313 K from 1 to 40 bar at two relevant gas compositions: $80H_2/20CO_2$ and $60H_2/40CO_2$. Figure 4 (A and B) compares the simulated PSA working capacities of **1** (using a desorption pressure of 1 bar) to the working capacities of the recently reported industrial benchmarks zeolite 13X and activated carbon JX101, and two of the top-performing MOFs identified for this application, MgMOF-74 and Cu-BTTri (*23*). A similar comparison of the CO_2/H_2 selectivities is given in Fig. 4 (C and D) at the two H_2/CO_2 ratios (table S7). At low CO_2 concentrations (80% H_2 and 20% CO_2), **1** has the largest working capacity of up to an adsorption pressure of 15 bar but remains among the top performers in this respect throughout the pressure range (*51*). Only the MOF Cu-BTTri has a significantly higher working capacity at pressures greater than 25 bar. However, Cu-BTTri has a very poor H_2/CO_2 selectivity, the lowest of all the materials compared, making it unsuitable for practical use (*23*). At higher CO_2 concentrations (60% H_2 and 40% CO_2), the working capacity of **1** is less competitive. Nonetheless, when compared to zeolite 13X, which is used industrially for PSA-based CO_2 scrubbing of natural gas, **1** has an almost identical selectivity but roughly double the working capacity throughout the pressure range. Compared to the high-performance activated carbon JX101, **1** has a higher working capacity for the 80:20 gas mixture and a comparable working capacity for the 60:40 gas mixture throughout the whole pressure range. However, **1** has a CO_2/H_2 selectivity that is at least 2.5 times better than JX101 for both gas compositions. Figure 4 shows that MgMOF-74 has one of the highest working capacities at all pressures and both gas compositions. Moreover, in all cases, it also has the highest CO_2/H_2 selectivity, outperforming Ni-4PyC by at least 50% in this respect. Despite the favorable adsorption properties, MgMOF-74 is not hydrolytically stable due to the presence of open metal sites, which limits its practical use. We note that **1** has one of the highest reported CO_2/H_2 selectivities of MOFs reported in the literature (see table S11 in the Supplementary Materials).

Ni-4PyC exhibits exceptional stability and recyclability properties, which are critical attributes of solid sorbents when used in industrial PSA systems. A sample of **1** was exposed to steam for 160 hours, and the powder x-ray diffraction (PXRD) pattern remains essentially unchanged as shown in Fig. 5A (blue and magenta patterns). In another key experiment, **1** was maintained under a constant stream of humidified CO_2 [~30% relative humidity (RH)] for over 48 hours. Figure 5B reveals that the CO_2 adsorption isotherms are the same before and

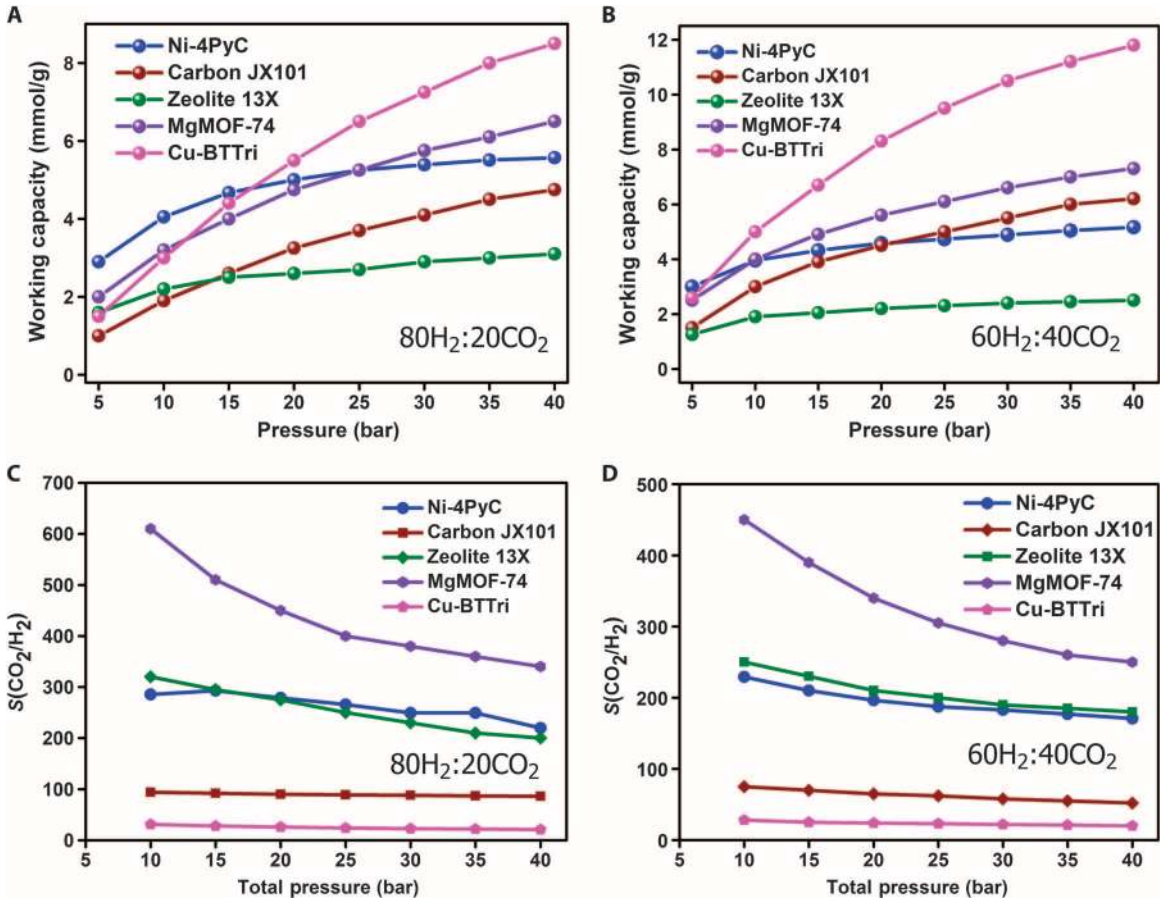

Fig. 4. Working capacities and selectivity characteristics. (**A** and **B**) The working capacity of **1** determined from simulation compared to that of several industrial sorbents and MOFs determined from (i) $80H_2/20CO_2$ and (ii) $60H_2/40CO_2$ gas mixtures at 313 K. The working capacities have been evaluated using a desorption pressure of 1 bar. (**C** and **D**) Comparison of the H_2/CO_2 selectivity of **1** versus other known MOFs and industrial sorbents determined from (i) $80H_2/20CO_2$ and (ii) $60H_2/40CO_2$ gas mixtures at 313 K. Data for activated carbon JX101, zeolite 13X, MgMOF-74, and Cu-BTTri are taken from the study of Herm *et al.* (*23*).

after this treatment. Also, a water vapor isotherm and a post-adsorption PXRD further support **1**'s hydrolytic stability (fig. S25). Even harsher humidity treatments did not seem to reduce the CO_2 capacity of **1** (figs. S26 and S27). The exceptional hydrolytic stability of **1** is accompanied by an excellent hydrostatic stability (*52*). **1** was found to retain its original porous structure after being subjected to 70-bar pressure for 24 hours as shown by the PXRD patterns given in Fig. 5A (blue and green patterns). In terms of shelf life, we found that **1** retains >90% of its porosity even after exposure to ambient air for over 6 months (fig. S29).

1 has smooth adsorption-desorption characteristics as observed from thermogravimetric analysis (TGA) cycling experiments, the results of which are shown in Fig. 5C. In these experiments, the CO_2 uptake is cycled up to ~6.5% by weight at 35°C. This easy removal of CO_2 is attributable to the moderate interactions of CO_2 with the framework (HOA, 25 to 30 kJ/mol, optimal for a pressure swing) (*41*). These cycling experiments produce the same results if He is used as a sweep gas.

When used as a solid sorbent in a PSA system, the small pores of an ultra-microporous MOF may severely restrict the adsorption and desorption times under practical operating conditions. This necessitates an investigation of the kinetics associated with the diffusion of CO_2 within the pores of **1**. A high-resolution rate of adsorption measurement was carried out using the ASAP 2020 HD instrument at 273 K in the pressure range of 0 to 1 bar, and eight different pressure points were used to determine the diffusion coefficients by fitting them against a spherical pore model (fig. S31) (*53*). From this single-component adsorption, an average diffusion coefficient of 3.03×10^{-9} m^2 s^{-1} for CO_2 was obtained (Fig. 5D). Meanwhile, the simulations gave a diffusion coefficient of 3.73×10^{-9} m^2 s^{-1} at 298 K under the flue gas compositions (fig. S31). This diffusivity is comparable to those observed in some of the microporous MOFs: ZIF-8, 8×10^{-10}; MIL-53(Cr), ~5×10^{-8}; MOF-5, 1.17×10^{-9}; and MOF-177, 2.3×10^{-9} m^2 s^{-1} at 298 K (*54*–*58*). The diffusion coefficient of **1** is also two orders of magnitude higher than that of zeolite 13X, which is currently used in PSA scrubbers for natural gas purification (*56*, *58*). When the CO_2 self-diffusion coefficient was measured using a pelletized form of **1**, only a little drop in its value was observed (1.66×10^{-9} m^2 s^{-1}, Fig. 5D).

To further verify the adsorption of CO_2 from a binary gas mixture, we carried out adsorption breakthrough measurements using 60% H_2/40% CO_2 and 60% He/40% CO_2 mixtures on a Rubotherm VariPSA system

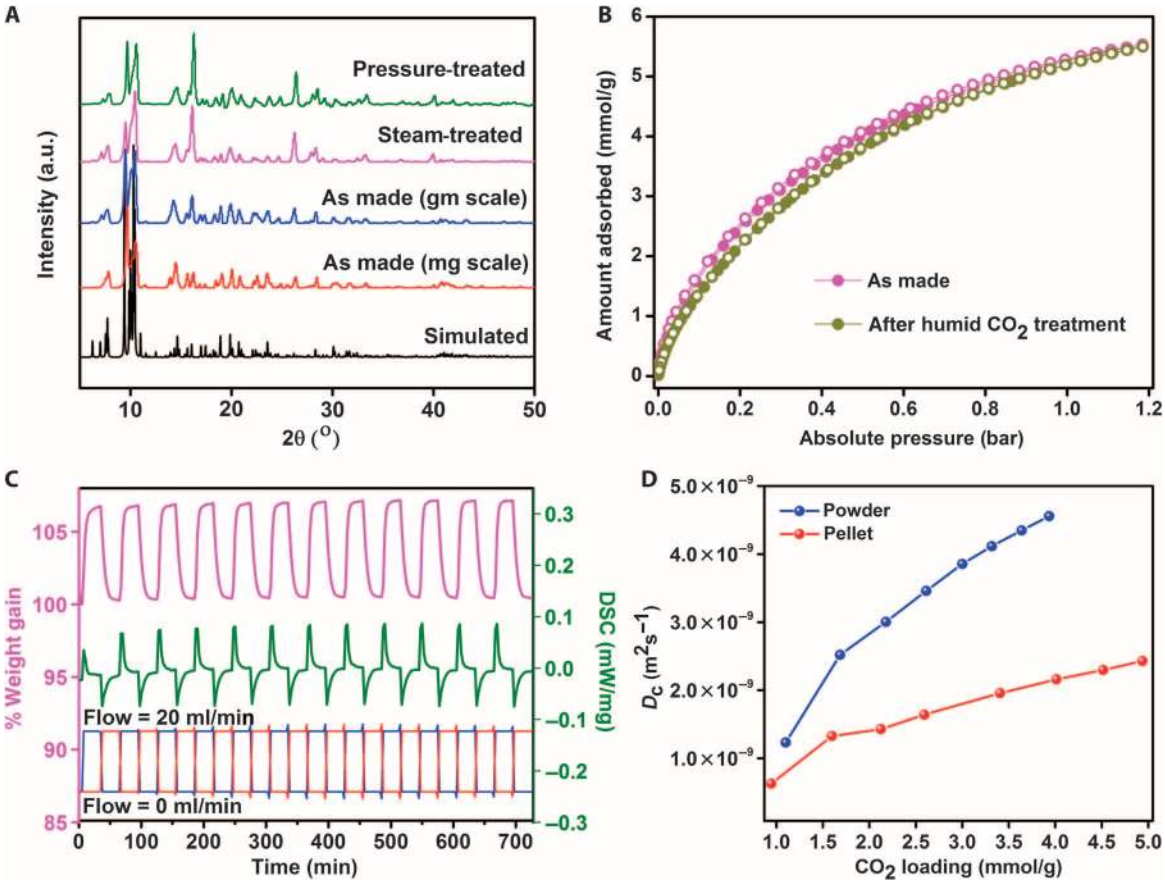

Fig. 5. Stability and CO_2 self-diffusion kinetics. (**A**) PXRDs showing the hydrolytic, hydrostatic stabilities and the homogeneity of the milligram- and gram-scale syntheses of **1**. (**B**) CO_2 adsorption isotherms of **1** at 273 K for as made and following exposure to humid (30% RH) CO_2 for 48 hours (filled circles, adsorption; open circles, desorption). (**C**) TGA cycling data on **1** carried out at 308 K. Blue, CO_2 flow; red, N_2 flow. DSC, differential scanning calorimetry. (**D**) Diffusion coefficient (D_c) as a function of CO_2 loading from eight loadings at 273 K for both the powder and pelletized forms of 1. Average diffusion coefficients for the powder and the pellet are 3.03×10^{-9} and 1.66×10^{-9} m^2 s^{-1}, respectively.

fitted with a nondispersive infrared sensor (see the Supplementary Materials for details). Multiple temperature sensors placed along the sample chamber indicated the noticeable rise in column temperature accompanying the CO_2 adsorption. The complete breakthrough of CO_2 was indicated by the downstream gas composition reaching that of the feed gas. The breakthrough profiles and CO_2 retention times for both gas mixtures were similar, indicating good selectivity for CO_2 over H_2 (Fig. 6). Also, when the column dimensions and the flow rates are normalized, the CO_2 retention times are comparable to those observed for other ultra-microporous MOFs (*31*). However, because of the lack of a direct method to determine the concentrations of H_2 adsorbed, quantitative measurements of CO_2/H_2 selectivity were not possible.

The laboratory gram-scale synthesis is becoming a norm as a potential prerequisite for a future large-scale synthesis (*42*). The initial 150-mg solvothermal synthesis of **1** could easily be scaled up to about 10 to 25 g via a simple procedure (see Materials and Methods). This makes the single ligand MOF **1** an attractive candidate for the kilogram-level scale-ups necessary for actual PSA applications. In contrast, multi-ligand synthesis often leads to the challenge of competing phases precipitating from a one-pot mixture, which is a serious impediment to large-scale synthesis. Some of the most widely researched and commercially sold MOFs such as HKUST-1, MOF-5, SNU, ZIF, MIL, and PCN series are made up of a single ligand (*59*).

DISCUSSION

Ni-4PyC, **1**, serves as an excellent prototype for demonstrating how an ultra-microporous MOF built from a small and readily available ligand can have highly favorable adsorption/desorption characteristics for gas separation processes, despite having pores <6 Å in size and a modest surface area (945 m^2/g). **1** has working capacities and CO_2/H_2 selectivities for PSA-based precombustion CO_2 capture that are competitive with the best-known MOFs for that application. Simulations of the CO_2 adsorption in **1** suggest that strong cooperative guest-guest interactions, in part, allow for the exceptional 8.2 mmol/g CO_2 uptake capacity of **1** at 10 bar and 298 K. In addition to having favorable gas adsorption properties, Ni-4PyC also exhibits excellent stability and recyclability—properties that are critical for practical operation in gas separation processes. Following 160 hours of steam treatment and 24 hours of exposure to 70-bar pressure, Ni-4PyC structure remains unchanged. Moreover, **1** retains its CO_2 adsorption properties following exposure to water. The simple, single-ligand synthesis

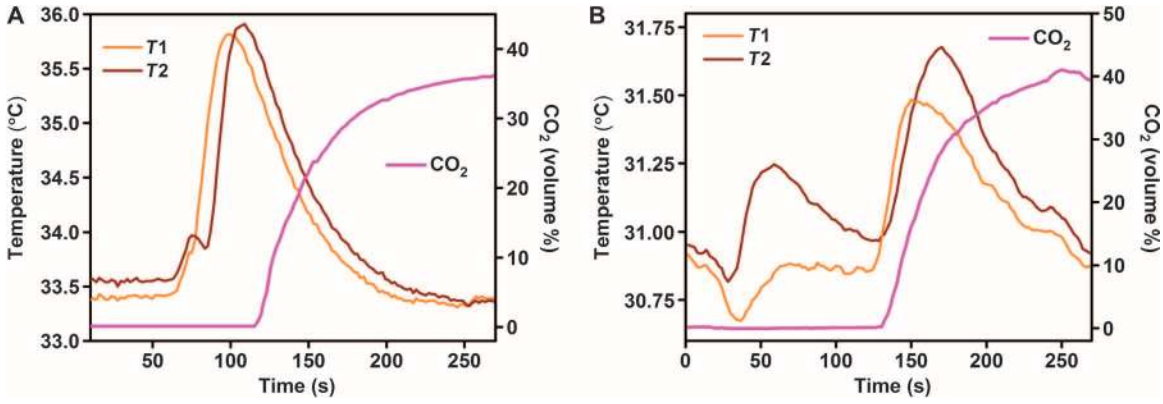

Fig. 6. Breakthrough measurements for CO_2-H_2 mix. (**A**) Breakthrough curve for the 60% H_2/40% CO_2 binary component mixture measured at 298 K and 1 bar. (**B**) Breakthrough curve for the 60% He/40% CO_2 binary component mixture measured at 298 K and 1 bar. *T*1 and *T*2 represent the bed temperatures measured at two points along the column (adsorption front).

and isolation to the gram scale suggests that potential industrial-level scale-ups should also be straightforward. With all these features and considering that **1** is built from inexpensive and readily available components, it is an attractive candidate for a variety of hydrogen purification applications. Such comprehensive performance with clear synthetic advantages from **1** should prompt revisiting ultra-microporous MOFs using small ligands as a design target for solid sorbents for gas separation applications.

MATERIALS AND METHODS

All the organic chemicals were purchased from Sigma-Aldrich. The nickel salts were procured from Alfa Aesar. Compounds and solvents were all used without any further purification.

Milligram-scale synthesis

A solvothermal reaction between nickel carbonate (0.119 g; 1 mmol) and pyridine-4-carboxylic acid (0.244 g; 2 mmol) in a solution containing 1.5 ml of tetrahydrofuran (THF) + 2.5 ml of water + 2 ml of MeOH was carried out at 150°C for 72 hours. A bright blue–colored polycrystalline product was isolated by filtration and was washed with plenty of water and methanol. The air-dried sample yielded ~85% (based on Ni). The PXRD pattern indicated this to be a pure phase of **1**. We have also prepared 10 to 25 g of this sample with an easy scale-up procedure. CHN analysis (calculated values within parentheses): C, 43.45% (43.22%); H, 3.62% (4.70%); N, 7.02% (7.08%). It was noted that the presence of THF was critical to the formation of this phase. However, it could be exchanged in a post-synthetic manner for methanol. Also, the use of nickel nitrate and other salts of nickel could not result in a pure phase of **1**. Initial pH 4.0; final pH ~5.0.

Gram-scale synthesis

About 2.975 g of anhydrous nickel carbonate was added to 6.1 g of 4-PyC in a solution containing 25 ml of water + 20 ml of MeOH + 10 ml of THF. The contents were stirred for 3 hours at room temperature, placed in a 123-ml Teflon-lined Parr stainless steel autoclave, and heated at 150°C for 72 hours. A bright blue–colored polycrystalline product identical in appearance to the smaller-scale preparation was obtained. The air-dried sample yielded ~87% (based on Ni). The PXRD, TGA, and N_2 and CO_2 gas uptakes matched well with the small-scale sample.

SUPPLEMENTARY MATERIALS

Supplementary material for this article is available at http://advances.sciencemag.org/cgi/content/full/1/11/e1500421/DC1

Materials and Methods
Single-crystal structure determination
Analytical characterizations
Adsorption analysis
Pore size determination from PALS
Virial
Simulation results: HOA, selectivities, and working capacities
Stability studies
Adsorption-desorption cycling experiments
Self-diffusion coefficient CO_2 in 1
Computational and molecular modeling details
Comparison of CO_2/H_2 selectivities of MOFs reported in the literature
Fig. S1. Comparison of the nickel clusters present in **1**, with the recently reported nickel clusters in pyridine carboxylate–based MOFs.
Fig. S2. Connolly surface representations of the nanoporous channels.
Fig. S3. PXRD of **1**, simulated versus as synthesized (milligram and gram scale).
Figs. S4 and S5. TGA of the as-made sample and the activated sample.
Fig. S6. Infrared spectra of **1**.
Fig. S7. CO_2 and N_2 adsorption isotherms of the milligram- and gram-scale syntheses.
Fig. S8. Fitting comparison obtained for the nonlocal DFT fit to the 195-K CO_2 data.
Fig. S9. Langmuir fits from the 195-K CO_2 data.
Fig. S10. BET and Langmuir fits from the 77-K N_2 data.
Fig. S11. Pore size distribution obtained from nonlocal DFT fit.
Fig. S12. PALS spectra of **1** at room temperature before and after the thermal annealing.
Fig. S13. HOA plots obtained from the virial fits and DFT analysis of the CO_2 isotherms.
Fig. S14. Comparison of experimental isotherms to the ones obtained from virial fits.
Fig. S15. Virial plots carried out using CO_2 isotherms at different temperatures.
Fig. S16. High-pressure H_2 isotherm at 298 K.
Fig. S17. Simulated HOA plots.
Fig. S18. CO_2/H_2 selectivity from ideal adsorbed solution theory.
Fig. S19. Pure-component working capacity.
Fig. S20. Simulated mixed-component isotherm for H2 purification and precombustion gas mixture.
Figs. S21 and S22. Mixed-component working capacities for a PSA (10 to 1 bar).
Figs. S23 and S24. Hydrolytic and thermal stability of **1** from PXRD.
Fig. S25. Hydrolytic stability evaluated from water vapor adsorption measurements.
Fig. S26. Hydrolytic stability from gas adsorption studies.
Fig. S27. Hydrolytic stability of **1** exposed to 80% RH at 80°C for 48 hours.
Fig. S28. Pressure-induced amorphization test from both PXRD and gas adsorption isotherms.
Fig. S29. Shelf life of **1** from gas adsorption isotherms.

Fig. S30. Comparison of the TGA cycling data for CO_2-N_2 cycling done on **1** and ZnAtzOx at 35°C.
Fig. S31. Modeling of diffusion kinetics of CO_2 in **1** from experiment and simulation.
Fig. S32. Plot of the mean square displacement of CO_2 from a molecular dynamics simulation for which a computed diffusion coefficient was estimated.
Fig. S33. A graphical representation of the solvent-accessible volume of **1**.
Fig. S34. Snapshots from an MD simulation of CO_2 diffusing from the cage to the channels.
Fig. S35. Comparison of the probability densities of CO_2 derived from GCMC simulations at 195 K and 1 bar and 298 K and 40 bar.
Table S1. CO_2 uptakes at 195 and 273 K for selected ultra- and microporous MOFs.
Table S2. CO_2 adsorption and desorption data at 195 K.
Table S3. Fitting results of **1** from PALS analysis.
Table S4. Summary of the fitted virial parameters.
Table S5. Uptakes and selectivities for the binary CO_2/H_2 (40:60) precombustion gas mixtures at a range of pressures.
Table S6. Uptakes and selectivities for the binary CO_2/H_2 (20:80) H_2 purification mixture at a range of pressures.
Table S7. Working capacities and selectivities for a PSA (10 to 1 bar) at 313 K at the relevant H_2/CO_2 gas mixtures for H_2 purification (80:20) and precombustion CO_2 capture (60:40) for integrated gasification combined cycle systems.
Table S8. Force field parameters used to model the H_2 guest molecules.
Table S9. Lennard-Jones parameters for framework atoms from the universal force field, CO_2 guest molecules.
Table S10. Cooperative CO_2-CO_2 energies with respect to the number of molecules loaded.
Table S11. H_2/CO_2 selectivities from literature.

REFERENCES AND NOTES

1. J. P. Longwell, E. S. Rubin, J. Wilson, Coal: Energy for the future. *Prog. Energy Combust. Sci.* **21**, 269–360 (1995).
2. *Coal: Medium-Term Market Report* (International Energy Agency, Paris, 2012 and 2014).
3. A. Samanta, A. Zhao, G. K. H. Shimizu, P. Sarkar, R. Gupta, Post-combustion CO_2 capture using solid sorbents: A review. *Ind. Eng. Chem. Res.* **51**, 1438–1463 (2012).
4. D. M. D'Alessandro, B. Smit, J. R. Long, Carbon dioxide capture: Prospects for new materials. *Angew. Chem. Int. Ed.* **49**, 6058–6082 (2010).
5. K. Liu, C. Song, V. Subramani, *Hydrogen and Syngas Production and Purification Technologies* (Wiley-AIChE, Hoboken, NJ, 2010), pp. 414–450.
6. D. A. J. Rand, R. M. Dell, *Hydrogen Energy: Challenges and Prospects* (RSC Energy Series, The Royal Society of Chemistry, Cambridge, 2008).
7. S. Mukherjee, P. Kumar, A. Hosseini, A. Yang, P. Fennell, Comparative assessment of gasification based coal power plants with various CO_2 capture technologies producing electricity and hydrogen. *Energy Fuels* **28**, 1028–1040 (2014).
8. A. Agarwal, L. T. Biegler, S. E. Zitney, Superstructure-based optimal synthesis of pressure swing adsorption cycles for precombustion CO_2 capture. *Ind. Eng. Chem. Res.* **49**, 5066–5079 (2010).
9. Q. Wang, Hydrogen production, in *Handbook of Climate Change Mitigation*, W.-Y. Chen, J. Seiner, T. Suzuki, M. Lackner, Eds. (Springer-Verlag, New York, 2012), pp. 1091–1130.
10. E. D. Akten, R. Siriwardane, D. S. Sholl, Monte Carlo simulation of single- and binary-component adsorption of CO_2, N_2, and H_2 in zeolite Na-4A. *Energy Fuels* **17**, 977 (2003).
11. D. Cao, J. Wu, Modeling the selectivity of activated carbons for efficient separation of hydrogen and carbon dioxide. *Carbon* **43**, 1364–1370 (2005).
12. S. Sircar, T. C. Golden, Purification of hydrogen by pressure swing adsorption. *Sep. Sci. Technol.* **35**, 667–687 (2000).
13. J.-R. Li, Y. Ma, M. C. McCarthy, J. Sculley, J. Yu, H.-K. Jeong, P. B. Balbuena, H.-C. Zhou, Carbon dioxide capture-related gas adsorption and separation in metal-organic frameworks. *Coord. Chem. Rev.* **255**, 1791–1823 (2011).
14. H. Furukawa, K. E. Cordova, M. O'Keeffe, O. M. Yaghi, The chemistry and applications of metal-organic frameworks. *Science* **341**, 1230444 (2013).
15. H.-C. J. Zhou, S. Kitagawa, Metal–organic frameworks (MOFs). *Chem. Soc. Rev.* **43**, 5415–5418 (2014).
16. Q. Liu, L. Ning, S. Zheng, M. Tao, Y. Shi, Y. He, Adsorption of carbon dioxide by MIL-101(Cr): Regeneration conditions and influence of flue gas contaminants. *Sci. Rep.* **3**, 2916 (2013).
17. S. Yang, X. Lin, W. Lewis, M. Suyetin, E. Bichoutskaia, J. E. Parker, C. C. Tang, D. R. Allan, P. J. Rizkallah, P. Hubberstey, N. R. Champness, K. M. Thomas, A. J. Blake, M. Schröder, A partially interpenetrated metal–organic framework for selective hysteretic sorption of carbon dioxide. *Nat. Mater.* **11**, 710–716 (2012).
18. A. L. Dzubak, L.-C. Lin, J. Kim, J. A. Swisher, R. Poloni, S. N. Maximoff, B. Smit, L. Gagliardi, Ab initio carbon capture in open-site metal–organic frameworks. *Nat. Chem.* **4**, 810–816 (2012).
19. J. A. Mason, K. Sumida, Z. R. Herm, R. Krishna, J. R. Long, Evaluating metal–organic frameworks for post-combustion carbon dioxide capture via temperature swing adsorption. *Energy Environ. Sci.* **4**, 3030–3040 (2011).
20. A. Andersen, S. Divekar, S. Dasgupta, J. H. Cavka, Aarti, A. Nanoti, A. Spjelkavik, A. N. Goswami, M. O. Garg, R. Blom, On the development of Vacuum Swing adsorption (VSA) technology for post-combustion CO_2 capture. *Energy Procedia* **37**, 33–39 (2013).
21. S. Xiang, Y. He, Z. Zhang, H. Wu, W. Zhou, R. Krishna, B. Chen, Microporous metal-organic framework with potential for carbon dioxide capture at ambient conditions. *Nat. Commun.* **3**, 954 (2012).
22. J. M. Huck, L.-C. Lin, A. H. Berger, M. N. Shahrak, R. L. Martin, A. S. Bhown, M. Haranczyk, K. Reuter, B. Smit, Evaluating different classes of porous materials for carbon capture. *Energy Environ. Sci.* **7**, 4132–4146 (2014).
23. Z. R. Herm, J. A. Swisher, B. Smit, R. Krishna, J. R. Long, Metal–organic frameworks as adsorbents for hydrogen purification and precombustion carbon dioxide capture. *J. Am. Chem. Soc.* **133**, 5664–5667 (2011).
24. Y. He, S. Xiang, Z. Zhang, S. Xiong, C. Wu, W. Zhou, T. Yildirim, R. Krishna, B. Chen, A microporous metal–organic framework assembled from an aromatic tetracarboxylate for H_2 purification. *J. Mater. Chem. A* **1**, 2543–2551(2013).
25. S. Reddy, S. Vyas, Recovery of carbon dioxide and hydrogen from PSA tail gas. *Energy Procedia* **1**, 149–154 (2009).
26. Q. Yang, Q. Xu, B. Liu, C. Zhong, B. Smit, Molecular simulation of CO_2/H_2 mixture separation in metal-organic frameworks: Effect of catenation and electrostatic interactions. *Chinese J. Chem. Eng.* **17**, 781–790 (2009).
27. C.-t. Chou, F.-h. Chen, Y.-J. Huang, H.-s. Yang, Carbon dioxide capture and hydrogen purification from synthesis gas by pressure swing adsorption. *Chem. Eng. Trans.* **32**, 1855–1860 (2013).
28. A. C. Kizzie, A. G. Wong-Foy, A. J. Matzger, Effect of humidity on the performance of microporous coordination polymers as adsorbents for CO_2 capture. *Langmuir* **27**, 6368–6373 (2011).
29. D. Saha, S. Deng, Structural stability of metal organic framework MOF-177. *J. Phys. Chem. Lett.* **1**, 73–78 (2010).
30. J. Yu, P. B. Balbuena, Water effects on postcombustion CO_2 capture in Mg-MOF-74. *J. Phys. Chem. C* **117**, 3383–3388 (2013).
31. P. Nugent, Y. Belmabkhout, S. D. Burd, A. J. Cairns, R. Luebke, K. Forrest, T. Pham, S. Ma, B. Space, L. Wojtas, M. Eddaoudi, M. J. Zaworotko, Porous materials with optimal adsorption thermodynamics and kinetics for CO_2 separation. *Nature* **495**, 80–84 (2013).
32. R. Vaidhyanathan, S. S. Iremonger, G. K. H. Shimizu, P. G. Boyd, S. Alavi, T. K. Woo, Direct observation and quantification of CO_2 binding within an amine-functionalized nanoporous solid. *Science* **330**, 650–653 (2010).
33. M. Bosch, M. Zhang, H.-C. Zhou, Increasing the stability of metal-organic frameworks. *Adv. Chem.* **2014**, 182327 (2014).
34. M. Dincă, A. F. Yu, J. R. Long, Microporous metal–organic frameworks incorporating 1,4-benzeneditetrazolate: Syntheses, structures, and hydrogen storage properties. *J. Am. Chem. Soc.* **128**, 8904–8913 (2006).
35. J. M. Taylor, A. H. Mahmoudkhani, G. K. H. Shimizu, A tetrahedral organophosphonate as a linker for a microporous copper framework. *Angew. Chem. Int. Ed.* **46**, 795–798 (2007).
36. Y.-S. Bae, D. Dubbeldam, A. Nelson, K. S. Walton, J. T. Hupp, R. Q. Snurr, Strategies for characterization of large-pore metal-organic frameworks by combined experimental and computational methods. *Chem. Mater.* **21**, 4768–4777 (2009).
37. J. H. Cavka, S. Jakobsen, U. Olsbye, N. Guillou, C. Lamberti, S. Bordiga, K. P. Lillerud, A new zirconium inorganic building brick forming metal organic frameworks with exceptional stability. *J. Am. Chem. Soc.* **130**, 13850–13851 (2008).
38. S. B. Kalidindi, S. Nayak, M. E. Briggs, S. Jansat, A. P. Katsoulidis, G. J. Miller, J. E. Warren, D. Antypov, F. Corà, B. Slater, M. R. Prestly, C. Martí-Gastaldo, M. J. Rosseinsky, Chemical and structural stability of zirconium-based metal–organic frameworks with large three-dimensional pores by linker engineering. *Angew. Chem. Int. Ed.* **54**, 221–226 (2015).
39. D. Feng, K. Wang, J. Su, T.-F. Liu, J. Park, Z. Wei, M. Bosch, A. Yakovenko, X. Zou, H.-C. Zhou, A highly stable zeotype mesoporous zirconium metal–organic framework with ultralarge pores. *Angew. Chem. Int. Ed.* **54**, 149–154 (2015).
40. D. Zhao, D. Yuan, D. Sun, H.-C. Zhou, Stabilization of metal–organic frameworks with high surface areas by the incorporation of mesocavities with microwindows. *J. Am. Chem. Soc.* **131**, 9186–9188 (2009).
41. J. M. Simmons, H. Wu, W. Zhou, T. Yildirim, Carbon capture in metal–organic frameworks—A comparative study. *Energy Environ. Sci.* **4**, 2177–2185 (2011).
42. Q. Yang, S. Vaesen, F. Ragon, A. D. Wiersum, D. Wu, A. Lago, T. Devic, C. Martineau, F. Taulelle, P. L. Llewellyn, H. Jobic, C. Zhong, C. Serre, G. De Weireld, G. Maurin, A water stable metal–organic framework with optimal features for CO_2 capture. *Angew. Chem. Int. Ed.* **52**, 10316–10320 (2013).
43. G.-S. Yang, Y.-Q. Lan, H.-Y. Zang, K.-Z. Shao, X.-L. Wang, Z.-M. Su, C.-J. Jiang, Two eight-connected self-penetrating porous metal–organic frameworks: Configurational isomers caused by different linking modes between terephthalate and binuclear nickel building units. *CrystEngComm* **11**, 274–277 (2009).
44. S. A. Kumalah, K. T. Holman, Polymorphism and inclusion properties of three-dimensional metal-organometallic frameworks derived from a terephthalate sandwich compound. *Inorg. Chem.* **48**, 6860–6872 (2009).

45. Y.-B. Zhang, H.-L. Zhou, R.-B. Lin, C. Zhang, J.-B. Lin, J.-P. Zhang, X.-M. Chen, Geometry analysis and systematic synthesis of highly porous isoreticular frameworks with a unique topology. *Nat. Commun.* **3**, 642 (2012).
46. G. Jiang, T. Wu, S.-T. Zheng, X. Zhao, Q. Lin, X. Bu, P. Feng, A nine-connected mixed-ligand nickel-organic framework and its gas sorption properties. *Cryst. Growth Des.* **11**, 3713–3716 (2011).
47. M. Cortijo, S. Herrero, R. Jiménez-Aparicio, J. Perles, J. L. Priego, M. J. Torralvo, J. Torroba, Hybrid polyfunctional systems based on nickel(II) isonicotinate. *Eur. J. Inorg. Chem.* **2013**, 2580–2590 (2013).
48. M. Liu, A. G. Wong-Foy, R. S. Vallery, W. E. Frieze, J. K. Schnobrich, D. W. Gidley, A. J. Matzger, Evolution of nanoscale pore structure in coordination polymers during thermal and chemical exposure revealed by positron annihilation. *Adv. Mater.* **22**, 1598–1601 (2010).
49. P. Kirkegaard, M. Eldrup, Positronfit extended: A new version of a program for analysing position lifetime spectra. *Comput. Phys. Commun.* **7**, 401–409 (1974).
50. R. Vaidhyanathan, S. S. Iremonger, G. K. H. Shimizu, P. G. Boyd, S. Alavi, T. K. Woo, Competition and cooperativity in carbon dioxide sorption by amine-functionalized metal–organic frameworks. *Angew. Chem. Int. Ed.* **51**, 1826–1829 (2012).
51. We have used the same gas composition for the adsorption and desorption conditions, which provides an upper limit to the calculated working capacity. This is consistent with what has been previously reported and allows for comparison of the working capacities published for other materials.
52. K. W. Chapman, G. J. Halder, P. J. Chupas, Pressure-induced amorphization and porosity modification in a metal–organic framework. *J. Am. Chem. Soc.* **131**, 17546–17547 (2009).
53. K. Malek, M.-O. Coppens, Knudsen self- and Fickian diffusion in rough nanoporous media. *J. Chem. Phys.* **119**, 2801 (2003).
54. L. Zhang, G. Wu, J. Jiang, Adsorption and diffusion of CO_2 and CH_4 in zeolitic imidazolate framework-8: Effect of structural flexibility. *J. Phys. Chem. C* **118**, 8788–8794 (2014).
55. F. Salles, H. Jobic, A. Ghoufi, P. L. Llewellyn, C. Serre, S. Bourrelly, G. Férey, G. Maurin, Transport diffusivity of CO_2 in the highly flexible metal–organic framework MIL-53(Cr). *Angew. Chem. Int. Ed.* **48**, 8335–8339 (2009).
56. Z. Zhao, Z. Li, Y. S. Lin, Adsorption and diffusion of carbon dioxide on metal–organic framework (MOF-5). *Ind. Eng. Chem. Res.* **48**, 10015–10020 (2009).
57. D. Saha, Z. Bao, F. Jia, S. Deng, Adsorption of CO_2, CH_4, N_2O, and N_2 on MOF-5, MOF-177, and zeolite 5A. *Environ. Sci. Technol.* **44**, 1820–1826 (2010).
58. J. A. C. Silva, K. Schumann, A. E. Rodrigues, Sorption and kinetics of CO_2 and CH_4 in binderless beads of 13X zeolite. *Microporous Mesoporous Mater.* **158**, 219–228 (2012).
59. Basosiv M050 (magnesium formate), Basolite Z1200 (Zn-methylimidazole, ZIF-8), Basolite C300/F300 (Cu or Fe trimesate, HKUST-1), and Basolite A100 (aluminum terephthalate, MIL-53) are all sold under Sigma-Aldrich trademark.

Acknowledgments

Funding: We acknowledge the Indian Institute of Science Education and Research (Pune), the Ministry of Human Resources and Development, and the Natural Sciences and Engineering Research Council of Canada for the necessary funding and support of the research. We thank Enovex Technology Corporation for supporting part of our instrumentation. S.N. thanks Science and Engineering Research Board–Confederation of Indian Industry–Department of Science and Technology and Enovex for supporting him through the Prime Minister Fellowship. We thank the Canada Foundation for Innovation for computing resources. **Author contributions:** S.N. performed the synthesis; carried out all the experimental work on porosity, CO_2 cycling, and stability investigations; and analyzed all the experimental results. P.D.L. and T.D.D. carried out the computational simulations and analysis. J.R. carried out the breakthrough measurements. M.L. and A.I.H. designed and carried out the PALS measurements and interpreted the data. W.B. assisted us with the experimental ideal adsorbed solution theory and diffusion calculations. R.V. conceived the idea, designed the experiments, and authored the manuscript. T.K.W. guided the direction of the work, designed the computational simulations and analysis, and authored the manuscript. **Competing interests:** The authors declare that they have no competing interests. **Data and materials availability:** All data needed to evaluate the conclusions in the paper are present in the paper and/or the Supplementary Materials. Additional data related to this paper may be requested from the authors.

Submitted 2 April 2015
Accepted 15 September 2015
Published 18 December 2015
10.1126/sciadv.1500421

Citation: S. Nandi, P. De Luna, T. D. Daff, J. Rother, M. Liu, W. Buchanan, A. I. Hawari, T. K. Woo, R. Vaidhyanathan, A single-ligand ultra-microporous MOF for precombustion CO_2 capture and hydrogen purification. *Sci. Adv.* **1**, e1500421 (2015).

Science Advances
AAAS

A single-ligand ultra-microporous MOF for precombustion CO 2 capture and hydrogen purification

Shyamapada Nandi, Phil De Luna, Thomas D. Daff, Jens Rother, Ming Liu, William Buchanan, Ayman I. Hawari, Tom K. Woo and Ramanathan Vaidhyanathan (December 18, 2015)
Sci Adv 2015, 1:.
doi: 10.1126/sciadv.1500421